

Discharge mode and particle transport in radio frequency capacitively coupled Ar/O_2 plasma discharges

Zhuo-Yao Gao(高卓瑶), Wan Dong(董婉), Chong-Biao Tian(田崇彪), Xing-Zhao Jiang(蒋星照), Zhong-Ling Dai(戴忠玲), and Yuan-Hong Song(宋远红)

Citation: Chin. Phys. B, 2024, 33 (**9**): 095203. DOI: 10.1088/1674-1056/ad5d65
Journal homepage: http://cpb.iphy.ac.cn; http://iopscience.iop.org/cpb

What follows is a list of articles you may be interested in

Experimental studies of H_2/Ar plasma in a cylindrical inductive discharge with an expansion region

Shi-Bo Li(李世博), Si-Yu Xing(邢思雨), Fei Gao(高飞), and You-Nian Wang(王友年)
Chin. Phys. B, 2024, 33 (**10**): 105201. DOI: 10.1088/1674-1056/ad6250

Calculation and prediction of divertor detachment via impurity seeding by using one-dimensional model

Wen-Jie Zhou(周文杰), Xiao-Ju Liu(刘晓菊), Xiao-He Wu(邬潇河), Bang Li(李邦), Qi-Qi Shi(石奇奇), Hao-Chen Fan(樊皓尘), Yan-Jie Yang(杨艳杰), and Guo-Qiang Li(李国强)
Chin. Phys. B, 2024, 33 (**8**): 085205. DOI: 10.1088/1674-1056/ad426a

Global dust density in two-dimensional complex plasma

Yi-Zhen Zhao(赵逸真), Song-Fen Liu(刘松芬), Wei Kong(孔伟), and Fang Yang(杨芳)
Chin. Phys. B, 2024, 33 (**6**): 065201. DOI: 10.1088/1674-1056/ad2a76

Simulation of deuterium pellet ablation and deposition in the EAST tokamak with HPI2 code

Da-Zheng Li(李大正), Jie Zhang(张洁), Ji-Lei Hou(侯吉磊), Mao Li(李懋), and Ji-Zhong Sun(孙继忠)
Chin. Phys. B, 2024, 33 (**4**): 045204. DOI: 10.1088/1674-1056/ad1e68

Electron characteristics and dynamics in sub-millimeter pulsed atmospheric dielectric barrier discharge

Junlin Fang(方骏林), Yarong Zhang(张亚容), Chenzi Lu(卢陈梓), Lili Gu(顾莉莉), Shaofeng Xu(徐少锋), Ying Guo(郭颖), and Jianjun Shi(石建军)
Chin. Phys. B, 2024, 33 (**1**): 015201. DOI: 10.1088/1674-1056/ad0118

Discharge mode and particle transport in radio frequency capacitively coupled Ar/O_2 plasma discharges

Zhuo-Yao Gao(高卓瑶), Wan Dong(董婉), Chong-Biao Tian(田崇彪),
Xing-Zhao Jiang(蒋星照), Zhong-Ling Dai(戴忠玲), and Yuan-Hong Song(宋远红)†

Key Laboratory of Materials Modification by Laser, Ion, and Electron Beams (Ministry of Education), School of Physics, Dalian University of Technology, Dalian 116024, *China*

(Received 31 March 2024; revised manuscript received 27 June 2024; accepted manuscript online 1 July 2024)

Simulations are conducted on capacitively coupled Ar/O_2 mixed gas discharges employing a one-dimensional fluid coupled with an electron Monte Carlo (MC) model. The research explores the impact of different O_2 ratio and pressures on the discharge characteristics of Ar/O_2 plasma. At a fixed Ar/O_2 gas ratio, with the increasing pressure, higher ion densities, as well as a slight increase in electron density in the bulk region can be observed. The discharge remains dominated by the drift–ambipolar (DA) mode, and the flux of O(^{3}P) at the electrode increases with the increasing pressure due to higher background gas density, while the fluxes of O(^{1}D) and Ar* decrease due to the pronounced loss rate. With the increasing proportion of O_2, a change in the dominant discharge mode from α mode to DA mode can be detected, and the O_2-associated charged particle densities are significantly increased. However, Ar^+ density shows a trend of increasing and then decreasing, while for neutral fluxes at the electrode, Ar* flux decreases, and O(^{3}P) flux increases with the reduced Ar gas proportion, while trends in O(^{1}D) flux show slight differences. The evolution of the densities of the charged particle and the neutral fluxes under different discharge parameters are discussed in detail using the ionization characteristics as well as the transport properties. Hopefully, more comprehensive understanding of Ar/O_2 discharge characteristics in this work will provide a valuable reference for the industry.

Keywords: Ar/O_2 mixed gas discharges, electron dynamics, transport of charged and neutral particles

PACS: 52.65.–y, 52.65.Ww, 52.80.Pi, 52.27.Cm **DOI:** 10.1088/1674-1056/ad5d65

1. Introduction

Radio frequency capacitively coupled plasmas (RF CCPs) play a vital role in large scale integrated circuit (LSIC) processes, such as plasma etching and plasma-enhanced chemical vapor deposition (PECVD).[1–3] When the plasma discharge occurs, electrons, ions, and neutral radicals are generated, and these particles can be utilized to interact with the surface materials for etching or surface material deposition.[3–7] This is due to the production of radicals, such as oxygen atoms, which oxidize polymers in high aspect ratio etching, reduce polymer barriers to ions, and accelerate ion etching of target materials. Meanwhile, the generated oxygen-related ions can also accelerate the etching process.[8,9] In the deposition process, these neutral radicals can serve as a source of oxygen-related precursors for depositing dielectric materials, such as SiO_2.[10,11]

A significant amount of research has been carried out in both industry and academics on the discharge of oxygen and its gas mixtures.[12–20] In academics, many studies have focused on the heating mechanism,[18–20] the discharge mode,[21,22] and the independent control of ion flux and energy.[20] Based on the particle-in-cell Monte Carlo collision (PIC/MCC) simulation, Wang *et al.*[22] found that there is a stronger reversal electric field near the sheath collapse phase in magnetized capacitively coupled radio frequency oxygen discharges. This field is caused by the reduction of the electron flux to the electrodes due to their trapping by the magnetic field and may be expected to affect the applications of such discharges in etching, deposition, and other semiconductor processing technologies. Moreover, in the oxygen discharge driven by tailored waveforms, a transition of the discharge mode from the drift-ambipolar (DA) mode to the α-mode is induced as a function of the consecutive harmonic number.[20] They also investigated neutral radical $O_2(a^1\Delta_g)$, and their simulations are compared with the experimental results, which further determines the quenching probability of $O_2(a^1\Delta_g)$ used in their study. Gudmundsson *et al.*[18] explored the electronegativity, and the electron heating mechanism in a single frequency capacitively coupled oxygen discharge using a one-dimensional PIC/MCC code. They found that electron heating within the plasma bulk (the electronegative core) dominates at 10 mTorr (1 Torr = 1.33322×10^2 Pa), but at 50 mTorr, sheath heating dominates. Based on the discharge parameter used in their paper, the electronegativity in the O_2 discharge is weakened as the pressure increases. On the other hand, in industry, the primary attention is typically given to the discharge characteristics which may have a direct impact on the performance of etching or deposition processes.[23–30] In the etching processes, it was found that the change in the Ar/O_2 ratio could effectively regulate the etching rate.[23,24] This is

†Corresponding author. E-mail: songyh@dlut.edu.cn

© 2024 Chinese Physical Society and IOP Publishing Ltd

because a change in the gas ratio effectively adjusts the ratio of reactive radicals and ions, which further changes the synergistic effect of the ions with the neutral radicals, and thus changes the etching rate. In addition, in the study of plasma treatment of silicon dioxide films,[25] O_2 equally plays an essential role. It was found that the concentration of O_2 controls the active species, reduces the impurity concentration, as well as enhances the effective working depth of the plasma. Moreover, during the deposition processes, studies have focused on O and metastable O atoms and have attempted to explore the possible effects of different oxygen atoms on the process. Kitajima *et al.*[26,27] found metastable O(^{1}D) atoms are believed to be one of the key factors of high quality SiO_2 film formation at low substrate temperatures because it has the potential to enhance the oxidation process. Therefore, they carried out a series of studies on O(^{1}D) in the Ar diluted O_2 plasma. And it is found that the O(^{1}D) atomic density does not increase linearly with the increase of O_2 ratio, and shows a trend of increasing and then decreasing, but the physical mechanisms in this phenomenon are not well understood. Oxidation of silicon with neutral atomic oxygen species generated in a rare gas plasma has recently been shown to produce high-quality thin oxides.[30] Therefore, it is necessary to carry out a series of studies on O_2 or its gas mixtures to understand the evolutions of ions, neutrals, and other particles as the discharge parameters change, which to some extent can provide parameter guidance for industry.

In this study, we investigate the electron dynamics and transport parameters of charged and neutral particles, in a single frequency capacitive discharge operated in Ar/O_2 gas mixtures, by using a one-dimensional (1D) fluid/electron MC hybrid model which can self-consistently consider both kinetic effects and more ions as well as neutrals in the reactive and electronegative gas mixtures. The article structure is as follows: Section 2 provides a concise overview of the simulation model. Section 3 delves into the results analysis, and concluding remarks are presented in the final section.

2. Model description

Discharges driven by single-frequency CCPs operated in Ar/O_2 gas mixtures at different pressures and different O_2 ratios are investigated using a 1D fluid model coupled with an electron MC model. In the fluid model, the continuity equation is used for electrons and ions, as shown in below:

$$\frac{\partial n_j}{\partial t} + \nabla \cdot \boldsymbol{\Gamma}_j = S_j, \tag{1}$$

where n_j is the density of species j, and $S_j = \sum_a k_{aj} n_a n_j$ is the source term in which k_{aj} is the rate coefficient for collisions between a and j. And, since the electron mass m_e is small and its inertial term can be neglected, the electron drift-diffusion approximation is adopted as

$$\boldsymbol{\Gamma}_e = -\frac{1}{m_e \nu_{en}} \left[e n_e \boldsymbol{E} + \nabla \left(n_e T_e \right) \right], \tag{2}$$

where e, T_e, and $\boldsymbol{E}$ are the elementary charge, electron temperature, and the electric field. The electron–neutral collision frequency is expressed by $\nu_{en} = k_{el-Ar} n_{Ar} + k_{el-O_2} n_{O_2}$, where n_{Ar} and n_{O_2} are the Ar and O_2 densities, and k_{el-Ar} and k_{el-O_2} obtained from the electron MC model are the momentum transfer coefficients between electrons and the background gas.

The ion temperature is kept at room temperature (about 400 K) for the cold fluid assumption, while their transport could be described by the momentum balance equation, as follows:

$$\begin{aligned} &\frac{\partial \left(n_\pm m_\pm \boldsymbol{u}_\pm \right)}{\partial t} + \nabla \cdot \left(n_\pm m_\pm \boldsymbol{u}_\pm \boldsymbol{u}_\pm \right) \\ &= -\nabla p + Z_\pm e n_\pm \boldsymbol{E} + M_\pm, \end{aligned} \tag{3}$$

where $\boldsymbol{\Gamma}_\pm$, $m_\pm$, $Z_\pm e$, and p represent the ion flux, ion mass, ion charge, as well as the pressure. The two items on the left side are the acceleration term and advection flux term. On the right side, we see the pressure gradient term, drift flux term due to the electric field force, and the source term due to the friction force (the specific equations are as follows: $M_\pm = -\frac{n_\pm m_\pm}{m_\pm + m_n} \boldsymbol{\Gamma}_\pm \nu_{i,n}$, where m_n, $\nu_{i,n}$ represent the ion–neutral momentum transfer frequency, the neutral mass).

The combination of the neutral continuity and diffusion equation yields Eq. (4), which can be used to describe the neutral density and transport, as

$$\frac{\partial n_n}{\partial t} + \nabla \cdot \left(-D_n \nabla n_n \right) = S_n, \tag{4}$$

where D_n and S_n are the diffusion coefficient and source term. Here, based on the Blanc law, the diffusion coefficient D_n of neutral species n is determined by the corresponding coefficients in the background gas Ar and O_2. The detailed expression of D_n can be found in Ref. [31], in which the binary collision diameters (σ_i) and potential energies (ε_i/k_b) are given in Table 1.

Table 1. Lennard–Jones parameters and viscosity coefficient of neutral particles.

Neutrals	σ_i (Å)	ε_i/k_b (K)	η_i
Ar*	3.542	93.3	0.8[32]
O(^{3}P)	3.05	106.7	0.1[33,34]
O(^{1}D)	3.05	106.7	0.1[35]
$O_2(a^1\Delta_g)$	2.44	113.0	0.007[36]

For each time step, the charged particle density is transferred to Poisson's equation to obtain the instantaneous electric potential and electric field distributions. After 5 RF cycles running in the fluid model, the stored instantaneous electric field information is transferred to the electron MC model. In the electron MC model, the electron motion with electric field will be tracked, and meanwhile the collision processes between the electron and the neutrals are included. And further,

the electron energy distribution function (EEDF) $f(\varepsilon,x,t)$ in space and time evolutions is statistically counted. The electron temperature $T_e(x,t)$ and the collision reaction rate coefficients $k_{e,j}(x,t)$ can be calculated using EEDF.[37,38]

$$E_e(x,t) = \int_0^\infty f(\varepsilon,x,t)\varepsilon \,\mathrm{d}\varepsilon, \tag{5}$$

$$T_e(x,t) = \frac{2}{3}\left(E_e(x,t) - \frac{1}{2}m_e u(x,t)u(x,t)\right), \tag{6}$$

$$k_{e,j}(x,t) = \int_0^\infty f(\varepsilon,x,t)\sigma_{e,j}(\varepsilon)\left(\frac{2\varepsilon}{m_e}\right)^{1/2} \mathrm{d}\varepsilon. \tag{7}$$

Equation (6) clarifies that the kinetic energy contributed by the directional velocity $u(x,t)$ should be subtracted from the total energy $E_e(x,t)$ to calculate the electron temperature $T_e(x,t)$. Equation (7) defines the reaction rate coefficient for the j-th collisional reaction between electrons and the corresponding neutral particles, where $\sigma_{e,j}$ and $(2\varepsilon/m_e)^{1/2}$ represent the j-th collision cross section and the electron velocity, respectively.

And then, these values are transferred to the fluid model. This process is repeated until the calculation reaches 3×10^4 RF cycles and each physical quantity converges to a definite value. At this stage, the calculation is finished and the particle density, electric field, and other relevant physical parameters are stored and exported. In this paper, the role of the secondary electron emission effect is not considered. These cases in this work utilize a single frequency source $V(t) = V_0\cos(2\pi ft)$, with a voltage V of 150 V and a frequency f of 13.56 MHz. The distance L between the two electrodes is fixed at 3 cm. The discharge pressures are 200, 300, and 500 mTorr and the oxygen ratios in the Ar/O_2 gas mixture range from 1% to 90%. More detailed information on the hybrid model, such as boundary conditions, electron reflection probability, *etc*., can be referred to our previous works.[37–39] In this paper, under the pressure of 200 mTorr–500 mTorr and the voltage of 150 V,[22,31] the role of the secondary electron emission effect is not taken into account since its limit effect.

In this work, there are 56 collision reactions considered in the reaction set of Ar/O_2 mixed gas, including elastic collisions, ionization collisions, excitation collisions, dissociative attachment collisions, as well as ion–ion collisions, ion–neutral collisions, neutral–neutral collisions, etc. Tables 2 and 3 show the specific information on the collision reactions, reaction thresholds, reaction rate coefficients, and references.[40–45] Five charged particles and four neutrals, including electron, Ar^+, O_2^+, O^+, O^-, Ar^*, $O(^3P)$, $O(^1D)$, $O_2(a^1\Delta_g)$, are taken into consideration. And the sticking coefficients for Ar^*, $O(^3P)$, $O(^1D)$, $O_2(a^1\Delta_g)$ are 0.8, 0.1, 0.1, 0.007,[32–36] respectively. Moreover, our calculation results are validated with the results of experiment under the same discharge conditions. The trends observed in the experimental and simulated results as a function of the gas ratio are almost consistent. This provides some indication of the reliability of the hybrid model and its reaction set.

Table 2. Electron–impact reactions considered in the model. By means of the cross-sections in the references, the corresponding rate coefficients are obtained on the basis of the MC method.

No.	Reactions	Threshold (eV)	Reference
R1	$e + Ar \rightarrow Ar + e$	0	[40]
R2	$e + Ar \rightarrow Ar^+ + 2e$	15.6	[41]
R3	$e + Ar \rightarrow Ar^* + e$	11.56	[41]
R4	$e + Ar^* \rightarrow Ar^+ + 2e$	4.14	[41]
R5	$e + Ar^* \rightarrow Ar + e$	–11.56	[41]
R6	$e + O_2 \rightarrow O_2 + e$	0	[42]
R7	$e + O_2 \rightarrow O_2\ (r>0) + e$	0.02	[42]
R8	$e + O_2 \rightarrow O_2\ (v=1) + e$	0.19	[42]
R9	$e + O_2 \rightarrow O_2\ (v=2) + e$	0.38	[42]
R10	$e + O_2 \rightarrow O_2\ (v=3) + e$	0.57	[42]
R11	$e + O_2 \rightarrow O_2\ (v=4) + e$	0.75	[42]
R12	$e + O_2 \rightarrow O_2^+ + 2e$	12.06	[42]
R13	$e + O_2 \rightarrow O(^3P) + O^-$	4.2	[42]
R14	$e + O_2 \rightarrow O_2\ (a^1\Delta_g) + e$	0.977	[42]
R15	$e + O_2 \rightarrow O_2\ (b^1\Sigma_g^+) + e$	1.63	[42]
R16	$e + O_2 \rightarrow O_2\ (A^3\Sigma_u^+, A^3\Delta_u, c^1\Sigma_u^-) + e$	4.5	[42]
R17	$e + O_2 \rightarrow O(^3P) + O(^3P) + e$	6.0	[42]
R18	$e + O_2 \rightarrow O(^3P) + O(^1D) + e$	8.4	[42]
R19	$e + O_2 \rightarrow O(^1D) + O(^1D) + e$	9.97	[42]
R20	$e + O_2 \rightarrow O(^3P) + O(3p^3P) + e$	14.7	[42]
R21	$e + O_2 \rightarrow O^+ + O(^3P) + 2e$	18.7	[43]
R22	$e + O(^3P) \rightarrow O(^1D) + e$	1.96	[42]
R23	$e + O(^3P) \rightarrow O^+ + 2e$	13.61	[42]
R24	$e + O(^1D) \rightarrow O^+ + 2e$	11.6	[42]
R25	$e + O(^1D) \rightarrow O(^3P) + e$	–1.96	[42]
R26	$e + O_2(a^1\Delta_g) \rightarrow O_2^+ + 2e$	11.08	[44]
R27	$e + O_2\ (a^1\Delta_g) \rightarrow O_2 + e$	–0.98	[44]
R28	$e + O_2(a_g^1) \rightarrow O(^3P) + O^-$		[44]
R29	$e + O_2(a^1\Delta_g) \rightarrow O(^3P) + O(^3P) + e$	5.14	[44]
R30	$e + O_2(a^1\Delta_g) \rightarrow O(^3P) + O(^1D) + e$	7.42	[44]
R31	$e + O_2(a^1\Delta_g) \rightarrow O(^1D) + O(^1D) + e$	8.99	[44]

Note: $O_2(r)$ denotes the rotationally excited state of O_2. $O_2(v1)$, $O_2(v2)$, $O_2(v3)$, $O_2(v4)$ denote the vibrationally excited states of O_2 with different excitation energy. $O_2(a^1\Delta_g)$, $O_2(b^1\Sigma_g^+)$, $O_2(A^3\Sigma_u^+, A^3\Delta_u, c^1\Sigma_u^-)$ indicate the products of O_2–electron excitation reactions. $O(^1D)$ is the excited state of atomic oxygen.

Table 3. Electron–ion, ion–ion, ion–neutral, and neutral–neutral reactions and their corresponding rate coefficients.

No.	Reactions	Reaction rate coefficient (cm^3/s)	Reference
R32	$e + O_2^+ \rightarrow O(^3P) + O(^3P)$	$1.20\times10^{-8}T_e^{-0.7}$	[45]
R33	$e + O_2^+ \rightarrow O(^3P) + O(^1D)$	$8.88\times10^{-9}T_{eZ}^{-0.7}$	[45]
R34	$e + O^+ \rightarrow O(^1D)$	$5.30\times10^{-13}T_e^{-0.5}$	[45]
R35	$e + O \rightarrow O(^3P) + 2e$	$1.95\times10^{-12}T_e^{-0.5}\exp(-3.4/T_e)$	[45]
R36	$Ar^+ + O_2 \rightarrow O_2^+ + Ar$	5.10×10^{-11}	[45]
R37	$Ar^+ + O(^3P) \rightarrow O^+ + Ar$	6.40×10^{-12}	[45]
R38	$O^+ + O(^3P) \rightarrow O(^3P) + O^+$	1.0×10^{-9}	[45]
R39	$O_2^+ + O_2 \rightarrow O_2 + O_2^+$	1.0×10^{-9}	[44]
R40	$O^+ + O_2 \rightarrow O(^3P) + O_2^+$	1.0×10^{-11}	[44]
R41	$O + O(^3P) \rightarrow O_2 + e$	2.0×10^{-10}	[44]
R42	$O_2^+ + O^- \rightarrow O(^3P) + O_2$	2.0×10^{-7}	[45]
R43	$O_2^+ + O^- \rightarrow O(^3P) + O(^3P) + O(^3P)$	1.0×10^{-7}	[45]
R44	$O + Ar^+ \rightarrow O(^3P) + Ar$	3.0×10^{-7}	[45]
R45	$O^- + O_2 \rightarrow O_3 + e$	5.0×10^{-15}	[45]
R46	$O^- + O_2(a^1\Delta_g) \rightarrow O_3 + e$	3.0×10^{-10}	[45]
R47	$O_2 + Ar^* \rightarrow O(^3P) + O(^3P) + Ar$	2.1×10^{-10}	[45]
R48	$O(^3P) + Ar^* \rightarrow O(^1D) + Ar$	4.1×10^{-11}	[45]
R49	$O(^1D) + Ar \rightarrow O(^3P) + Ar$	5.0×10^{-13}	[45]
R50	$O_2(a^1\Delta_g) + Ar \rightarrow O_2 + Ar$	1.0×10^{-19}	[45]
R51	$O(^1D) + O_2 \rightarrow O(^3P) + O_2(a^1\Delta_g)$	1.6×10^{-12}	[45]
R52	$O(^1D) + O(^3P) \rightarrow O(^3P) + O(^3P)$	8.0×10^{-12}	[45]
R53	$O(^1D) + O_2 \rightarrow O(^3P) + O_2$	4.8×10^{-12}	[45]
R54	$O_2(a^1\Delta_g) + O(^3P) \rightarrow O_2 + O(^3P)$	2.0×10^{-16}	[45]
R55	$O_2(a^1\Delta_g) + O_2 \rightarrow O_2 + O_2$	3.0×10^{-18}	[45]
R56	$O_2(a^1\Delta_g) + O_2(a^1\Delta_g) \rightarrow O_2 + O_2$	9.0×10^{-17}	[45]

3. Results and discussion

In this section, electron dynamics, and transport of charged and neutral particles will be studied in a capacitive RF plasma operated in Ar/O_2 (99/1∼10/90) at 200, 300, and 500 mTorr. The cosine voltage waveforms are employed at a frequency of 13.56 MHz and a voltage of 150 V. The electrodes are parallel to each other with a gap of 3 cm.

3.1. Effects of pressures on the electron dynamics

In this part, the gas ratio of the Ar/O_2 gas mixtures is fixed at 50/50 to investigate the effect of pressures on the discharge characteristics. Figure 1 illustrates the spatio-temporal evolutions of electron density (den.) and O^- density at 200, 300, and 500 mTorr. In electronegative discharges, negative ion tends to accumulate in the bulk region, while the electron density peaks appear at the sheath edges to maintain quasineutrality in the electropositive edge region of the discharge. The density distributions of electron and O negative ion in Fig. 1 closely are similar to those of typical electronegative gases with a 50/50 Ar/O_2 gas ratio. As the pressure increases from 200 mTorr to 300 mTorr and 500 mTorr, both the electron density and O^- density enhance. It is worth noting that the electron density at 500 mTorr is higher in the bulk region compared to those in the cases of 200 mTorr and 300 mTorr. Meanwhile, a slight change in the space–time averaged electronegativity can be observed, which shifts from 8.53 to 8.16 and 7.55, accordingly. This is mainly because with the increasing pressure, the density of background gas and the collision frequency increase, resulting in a higher probability of ionization and an increase in the electron density. The significant increase in electron density is the main reason for the decrease in electronegativity. It should be mentioned that the space–time averaged electronegativity of the discharge is defined as the ratio of the total number of negative ions (specifically O^- in this study) to electrons, calculated between the powered and grounded electrodes over one RF period. Besides, the electronegative behavior is similar to Gudmundsson *et al.*'s results.[18]

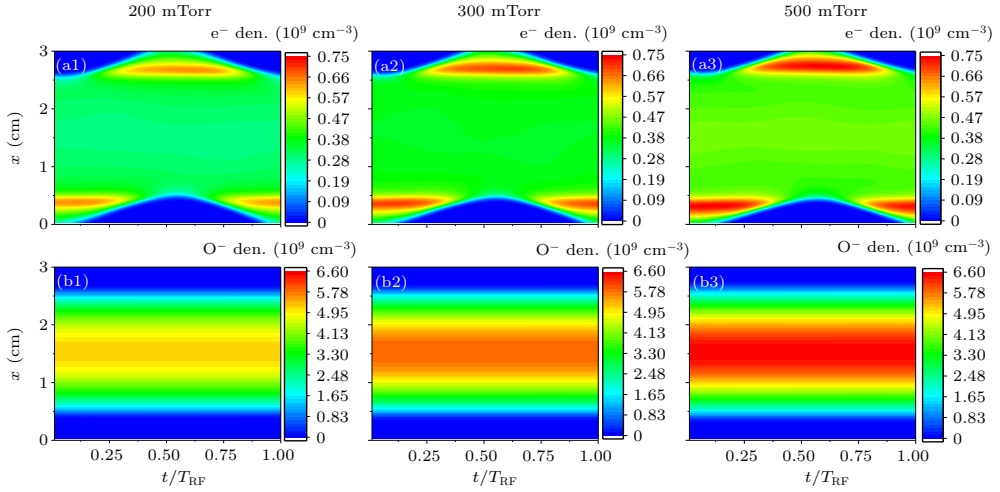


Fig. 1. Spatiotemporal evolutions of (a1)–(a3) electron density (den.), and (b1)–(b3) O^- density at 200, 300, and 500 mTorr. Discharge conditions: Ar/O_2 (50/50) mixed gases with an electrode gap of 3 cm, sustained by 13.56 MHz with 150 V voltage amplitude.

In Fig. 2, the spatial and temporal evolutions of the electric field, electron power absorption rate, and total ionization rate at 200, 300, and 500 mTorr are depicted. The electron power absorption rate is given by $-e\boldsymbol{\Gamma}_e\boldsymbol{E}$, where e is the electron charge, $\boldsymbol{\Gamma}_e$ is the electron flux, and $\boldsymbol{E}$ is the electric field. The total ionization rate encompasses the rates of reactions R2, R4, R12, R23, R24, R26, and R35 in the reaction set. Figure 3 displays the RF period-averaged EEDF as a function of pressure. From Fig. 2(a), there is a significant enhancement of the electric field in the bulk region. Taking the electric field at the phase of $0.75T_{RF}$, and the position of 1.5 cm as an example, its value enhances from 12.8 V/cm to 14.6 V/cm and 17.4 V/cm as the pressure increases. Besides, from the electron power absorption rate (Fig. 2(b)), the discharge operates at 200 mTorr, in which the sheath heating dominates. However, at pressures of 300 mTorr and 500 mTorr, the electron heating within the plasma bulk and sheath heating become almost comparable. Moreover, the electron heating of the bulk region is significantly enhanced at higher pressures. In general, stronger electron heating may lead to an enhancement in the ionization rate. But, with the increasing pressure, the discharges always show a DA mode since the electronegative gas O_2 is fixed at a higher proportion 50%, and the electronegativity is maintained at about 8. Meanwhile, there is a decrease in the ionization rate peaks, as shown in Fig. 2(c). From Fig. 3, as the pressure increases, there is a significant decrease in the number of high-energy electrons involved in ionization, which may be one of the reasons for the decrease in the peak ionization rate. Furthermore, another reason may be able to be discovered from the electron heating path. In electronegative gas discharges, electrons can be accelerated by the sheath expansion field, drift field in the bulk region, and ambipolar field at

the sheath collapse, obtaining sufficient energy. Consequently, intense ionization occurs in the vicinity of the sheath collapse. During this process, if the heating in the bulk region is strong enough, some of the electrons can gain enough energy in the bulk region to ionize. As depicted in Fig. 2(c), there is an increase in ionization in the bulk region at 300 mTorr and 500 mTorr compared to the case 200 mTorr. The depletion of high-energy electrons in the bulk region may also lead to a weakening of the ionization peak at the sheath collapse, which may be another reason. Although the peaks of the ionization rate decrease with the increasing pressure, the spatial and temporal distribution of the ionization rate expands significantly, potentially leading to an increase in electron density.

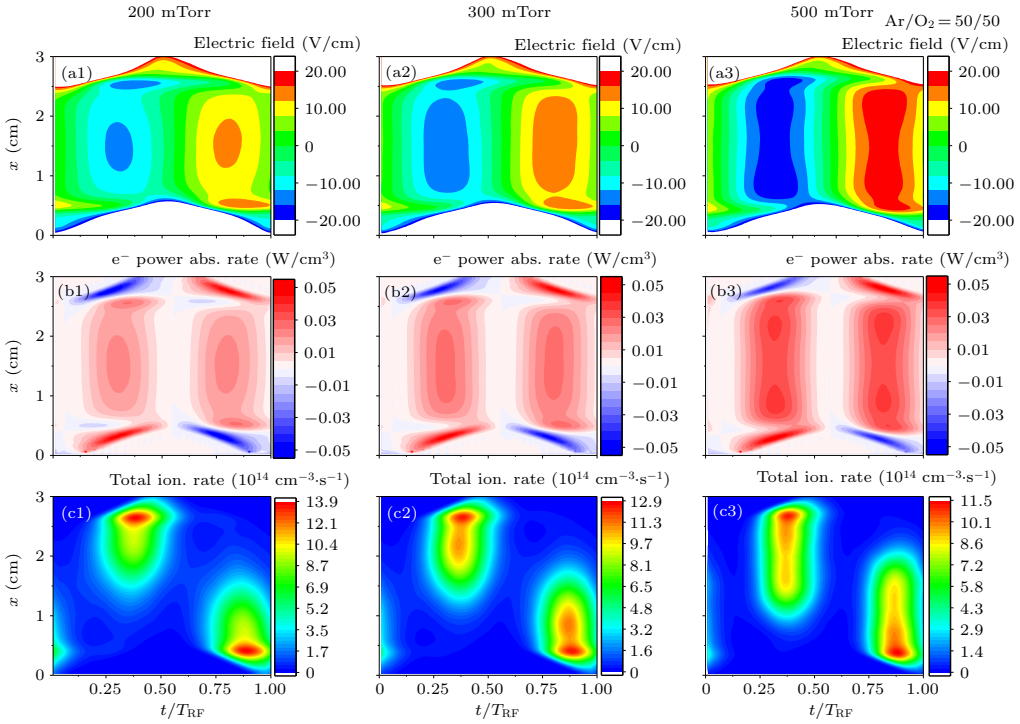


Fig. 2. Spatiotemporal evolutions of (a1)–(a3) electric filed, (b1)–(b3) electron power absorption (abs.) rate, and (c1)–(c3) total ionization (ion.) rate (the sum of the reaction rates of R2, R4, R12, R23, R24, R26, and R35) at 200, 300, 500 mTorr. The discharge conditions are the same as those in Fig. 1.

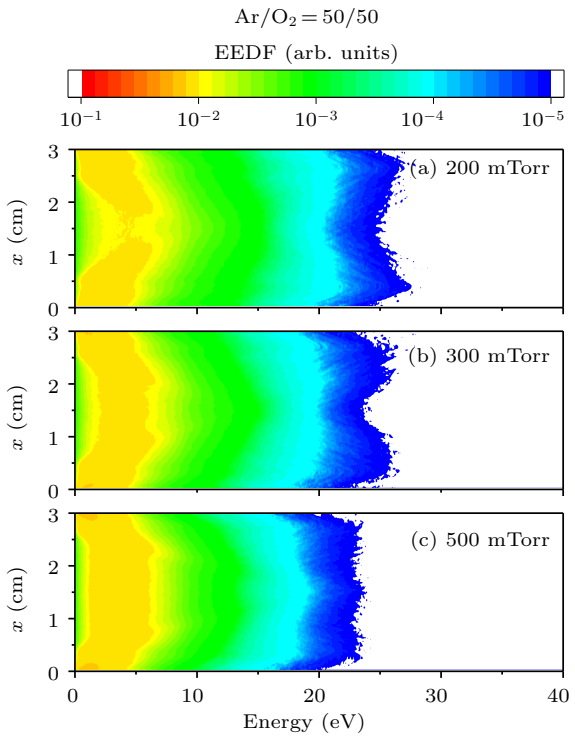


Fig. 3. RF period-averaged EEDF at (a) 200 mTorr, (b) 300 mTorr, and (c) 500 mTorr. The discharge conditions are the same as those in Fig. 1.

3.2. Effects of O_2 ratio on the electron dynamics

Figure 4 depicts the spatiotemporal evolutions of electron density and O^- density at a fixed pressure (200 mTorr), with O_2 ratio at 1%, 5%, 20%, and 50%. From Figs. 4(a1)–4(a4), there is a gradual transition in electron density from a predominantly concentrated in the bulk region to the sheath edge, which indicates a change in discharge characteristics from an electropositive-like mode to an electronegative mode, as the ratio of O_2 increases. Simultaneously, the density of O^- ions steadily rises and remains consistently distributed in the bulk region. Based on the above results, an increase of the space–time averaged electronegativity from 0.82 to 2.65, 5.47, and 8.53 can be obtained as the proportion of the electronegative gas O_2 rises from 1% to 5%, 20%, and 50%, respectively. Additionally, based on the simulation results, the threshold for the transition of discharge characteristics is determined to be approximately 2% O_2 ratio at a fixed pressure of 200 mTorr. At this gas ratio, the density of negative ions begins to exceed that of electrons, and the electron density near the sheath becomes higher than that in the bulk region. Moreover, if the pressure increases, the electronegativity will be declined. Consequently, the ratio of O_2 needs to be increased to find this threshold.

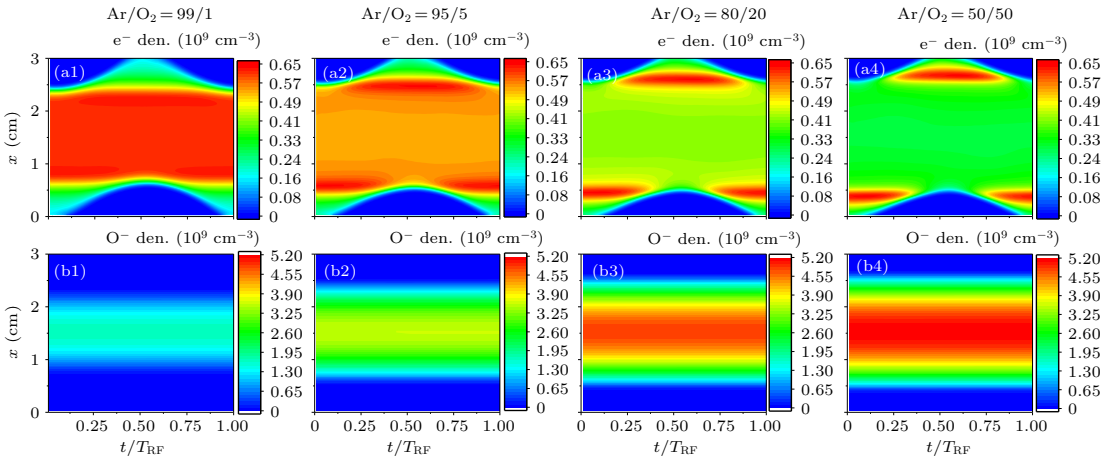


Fig. 4. Spatio-temporal evolutions of (a1)–(a4) electron density, and (b1)–(b4) O^- density as a function of O_2 gas ratio. Discharge conditions: Ar/O_2 (99/1, 99/5, 80/20, 50/50) mixed gases at 200 mTorr with an electrode gap of 3 cm, sustained by 13.56 MHz with 150-V voltage amplitude.

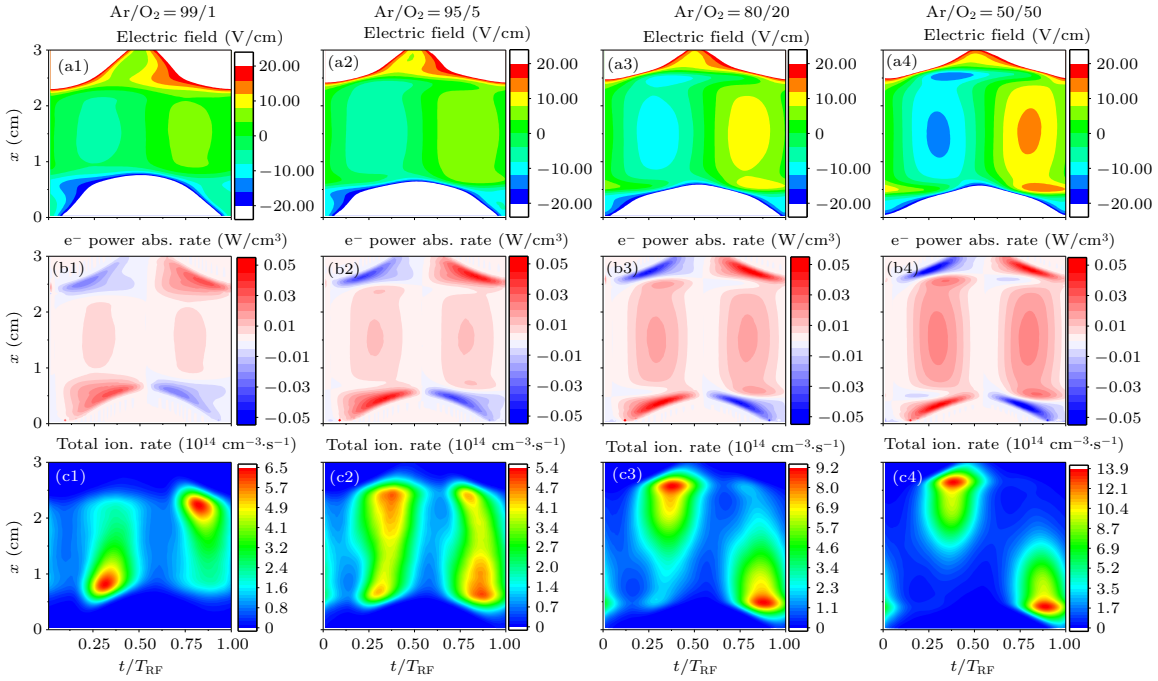


Fig. 5. Spatiotemporal evolutions of (a1)–(a4) electric filed, (b1)–(b4) electron power absorption (abs.) rate, and (c1)–(c4) total ionization (ion.) rate as a function of O_2 gas ratio. The discharge conditions are the same as those in Fig. 4.

In Fig. 5, spatiotemporal evolutions of the electric field, electron power absorption rate, and total ionization rate are presented as a function of O_2 gas ratio. The total ionization rate is similar to that demonstrated in Fig. 2(c), including the rates of reactions R2, R4, R12, R23, R24, R26, and R35. Figure 6 shows the RF period-averaged EEDF under different Ar/O_2 gas ratios of 99/1, 95/5, 80/20, and 50/50. From Fig. 5(a), the drift field and ambipolar field in the bulk region are observable gradually due to an enhancement in electronegativity and lower conductivity as the proportion of electronegative gas O_2 increases. The strength of the electric field will significantly affect the electron heating process. Figure 5(b) demonstrates that, at lower ratios of electronegative gas O_2 (1%–5%), electron heating in the sheath edge is dominant. However, at the Ar/O_2 gas ratio of 80/20, and 50/50, electron heating in the bulk region becomes significant enough to be comparable to that at the sheath edge. This will lead to an increase in the proportion of energetic electrons, as shown in Fig. 6. Further, the electron heating characteristics will affect the discharge mode as well as the ionization process. In Fig. 5(c1), at lower O_2 ratio, as the electron power absorption mode is mainly characterized by sheath heating, the α discharge mode is presented. When the oxygen proportion increases to 5%, the peaks of the ionization near the sheath collapse, and the sheath expansion phase becomes nearly equal. However, there is a slight decrease in the peak value of the ionization rate. This may be because, during the increase in the proportion of Ar from 99% to 95%, ionization occurs at both the sheath expansion and sheath collapse phase. Although the peaks of the ionization rate are smaller at an Ar/O_2 gas ratio

of 95/5, the space–time averaged ionization rate for an oxygen ratio of 5% is much larger than for that of 1%. As the proportion of O_2 increased to 20%, the discharge is operated in an electronegative mode. Despite the presence of weak ionization during the sheath expansion phase, the ionization is dominated by the DA mode, which is predominantly located near the sheath collapse and within the bulk region. At an Ar/O_2 gas ratio of 50/50, the ionization at the sheath expansion phase could not be observable, and only stronger ionization can be found in the bulk region and the vicinity of the sheath collapse phase. Besides, when the electronegative O_2 ratio increases further, the discharge mode remains essentially the same as shown in Fig. 5(c4), so the results are not shown here.

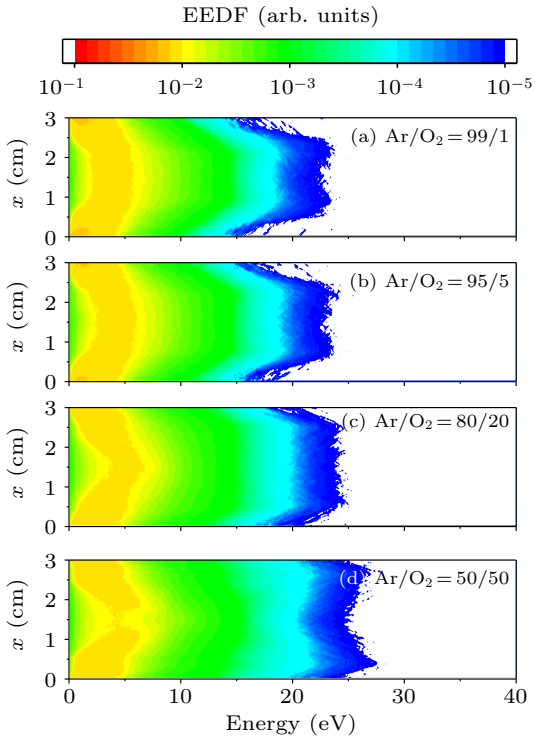


Fig. 6. RF period-averaged EEDF under different Ar/O_2 gas ratios of 99/1, 95/5, 80/20, and 50/50. The discharge conditions are the same as those in Fig. 4.

3.3. Charged particle densities and neutral fluxes at different pressures and O_2 ratio

To investigate the effects of changes in pressure and electronegative O_2 proportions on macroscopic physical parameters, such as the density of charged particles, figure 7 shows the space–time averaged electron density, total positive ions density (the sum of Ar^+ density, O^+ density, and O_2^+ density), O^- density, Ar^+ density, and electronegativity at different pressures and Ar/O_2 gas ratios. From Fig. 7, with the increasing pressure, densities of charged particles increase, while electronegativity (as discussed in Subsection 3.1) experiences a slight decrease at the same O_2 ratio. Simultaneously, the density of the background gas increases, which mean a reduction of the mean free path of electrons and an increase in collisions between electrons and neutrals, further leading to a substantial enhancement in both electron and ion densities. Moreover, as the proportion of electronegative O_2 gas increases, the trend of the results presented for the different pressure scenarios is almost the same. It shows that the electron density decreases, the O^- density and the total positive ion density first rise sharply and then in a slow increasing channel, and meanwhile the electronegativity enhances. Also, with the increase in electronegativity, the electric field in the bulk region is enhanced, the proportion of high-energy electrons increases, and the spatial and temporal distribution region of the ionization rate is enhanced, all of which leads to an increase in total positive ions density. Additionally, as the ratio of Ar decreases, the Ar^+ ion density shows an increasing and then decreasing trend, and reaches a maximum value at the O_2 ratio of 5% and a minimum value at the O_2 ratio of 90%. The trend in Ar^+ density is not as we expected. From Fig. 5(c), it can be seen that the peak of the ionization rate is slightly weakened, but the effective acting time and space of ionization has significantly increased accompanied by a shift in discharge mode from α to α-DA mode as the proportion of Ar is reduced from 99% to 95%. This may be the key factor contributing to the increase in Ar^+ density. Further, from Figs. 6(c) and 7, although the proportion of energetic electrons increases as the O_2 ratio increases from 5% to 50%, the Ar^+ density will decrease due to the continuous reduction of the Ar source and little variation in the effective acting time and space of ionization.

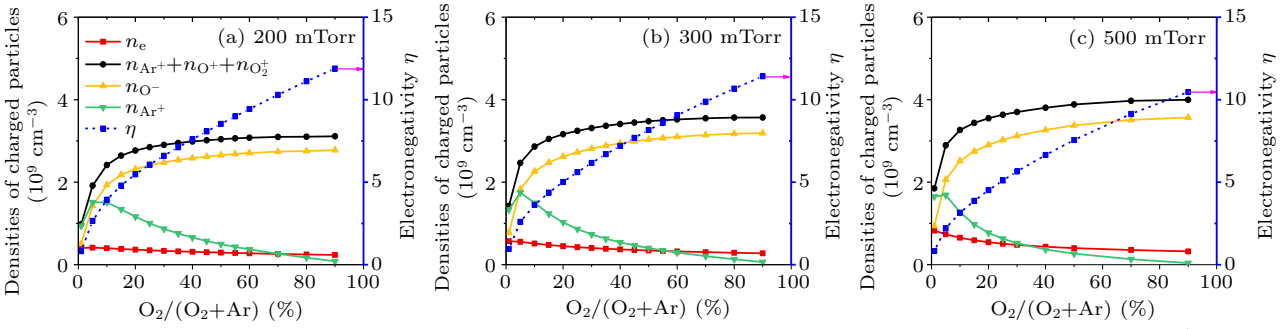


Fig. 7. Space–time averaged electron density (red line), total positive ions density (black line, the sum of Ar^+ density, O^+ density, and O_2^+ density), O^- density (orange line), Ar^+ density (green line), and electronegativity η at (a) 200 mTorr, (b) 300 mTorr, (c) 500 mTorr. Discharge conditions: Ar/O_2 (99/1∼10/90) mixed gases at 200, 300, and 500 mTorr with an electrode gap of 3 cm, sustained by 13.56 MHz with 150-V voltage amplitude.

In addition to the densities of charged particles, the fluxes of neutral particles near the powered electrode are concerned as well. Figure 8 presents the RF period-averaged fluxes of $O(^1D)$, $O(^3P)$, and Ar^* near the powered electrode at various pressures and gas ratios. As the pressure increases from 200 mTorr to 300 mTorr, and 500 mTorr, the flux of $O(^3P)$ increases, while the fluxes of $O(^1D)$ and Ar^* show a tendency of reduction. Changes in particle fluxes are generally associated with variations in the generation term or the loss term. Based on our computational results, R3 is the most dominant reaction for the generation of the Ar^*, the production of $O(^1D)$ is mainly related to the R18 reaction due to its larger reaction cross section, and the generation of $O(^3P)$ is dominated by reactions R18, R47. Besides, from Table 1, it can be observed that the thresholds of the above reactions (R3, R18) are basically maintained around 10 eV. From Fig. 3, the proportion of the electron in this energy range does not change significantly as the pressure increases. And further, with increasing pressure, their source term and neutral fluxes are supposed to increase because of the addition of more background gas. Except for $O(^3P)$ fluxes, the results of $O(^1D)$ and Ar^* in Fig. 9 are different from our expectations. This is mainly due to the fact that the increase in the densities of background gas (O_2 or Ar) with increasing pressure leads to an enhancement in the loss reaction source terms for $O(^1D)$ (such as R49, R53) and Ar^* (R47), which further results in a decline in the $O(^1D)$ and Ar^* densities.

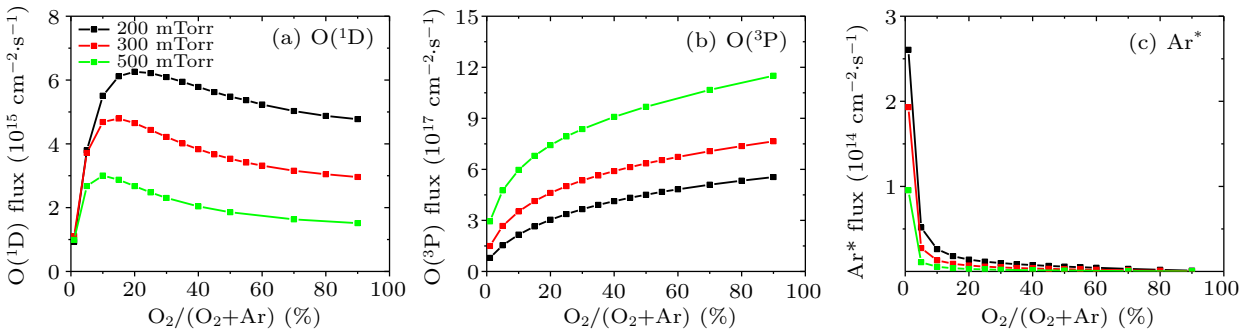


Fig. 8. RF period averaged fluxes of (a) $O(^1D)$, (b) $O(^3P)$, and (c) Ar^* at 200 (black line), 300 (red line), 500 (green line) mTorr near the powered electrode. Discharge conditions: Ar/O_2 (99/1∼10/90) mixed gases at 200, 300, and 500 mTorr with an electrode gap of 3 cm, sustained by 13.56 MHz with 150-V voltage amplitude.

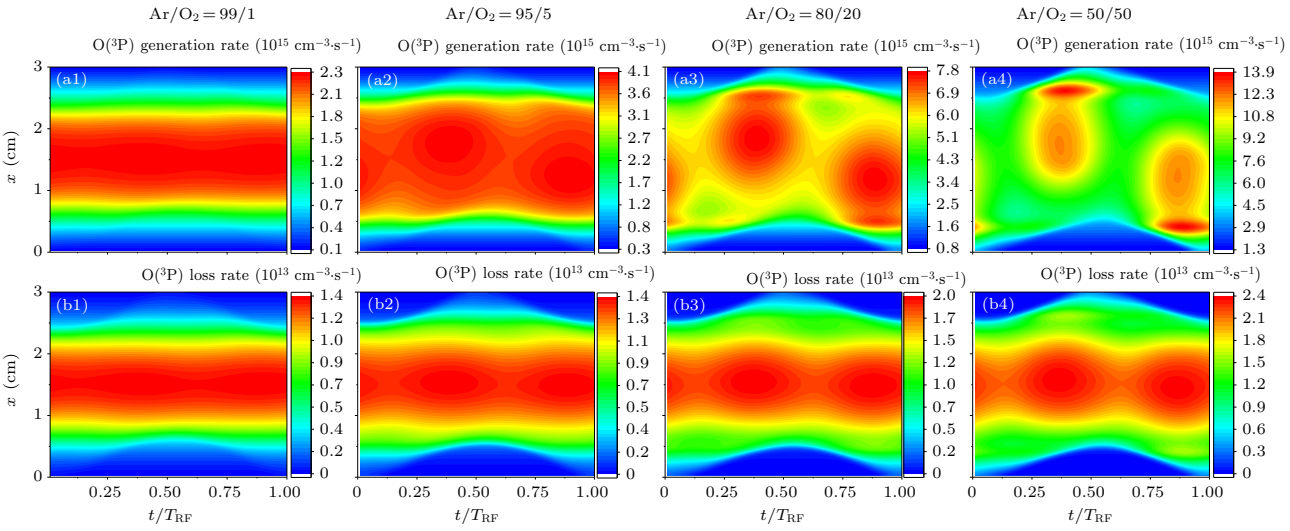


Fig. 9. Spatiotemporal evolutions of (a1)–(a4) $O(^3P)$ generation rate (the sum of the reaction rates of R13, R17, R18, R20, R21, R25, R28, R29, R30, R32, R33, R35, R40, R42, R43, R44, R47, R49, R51, R52, and R53), and (b1)–(b4) $O(^3P)$ loss rate (including the reaction rates of R22, R23, R37, R41, and R48) as a function of Ar/O_2 gas ratio (99/1, 95/5, 80/20, 50/50). Discharge conditions: Ar/O_2 mixed gases at 200 mTorr with an electrode gap of 3 cm, sustained by 13.56 MHz with 150-V voltage amplitude.

In addition, with an increase in the proportion of O_2 gas, there is a corresponding increase in the $O(^3P)$ flux and a decrease in the flux of Ar^*. This shift in gas composition leads to a higher flux of O_2-related particles and a lower flux of Ar-related particles. However, the $O(^1D)$ fluxes exhibit a trend of increasing and then decreasing, as shown in Fig. 8(a). To further investigate this phenomenon, taking the cases of 200 mTorr as an example, figures 9 and 10 show the space and time evolutions of $O(^3P)$ and $O(^1D)$ generation rate and loss rate at Ar/O_2 gas ratios of 99/1, 95/5, 80/20, and 50/50. From Fig. 9, it is evident that the peak values of the $O(^3P)$ generation rate significantly rise as the O_2 ratio increases from 1% to 5%, 20%, and 50%. The variation in the loss term of $O(^3P)$ is not pronounced com-

pared to the generation rate, leading to an increase in the flux of O(^{3}P) with higher proportions of O_2. From Fig. 10, the peak of the O(^{1}D) generation rate shows a substantial increase from 1.7×10^{14} cm^{-3}·s^{-1} to 8.1×10^{14} cm^{-3}·s^{-1}, 31.3×10^{14} cm^{-3}·s^{-1}, and 77.0×10^{14} cm^{-3}·s^{-1} as the O_2 ratio increases from 1% to 5%, 20%, and 50%. Meanwhile, the loss term of O(^{1}D) also changes significantly compared to that of O(^{3}P), with its peak increasing from 9.6×10^{13} cm^{-3}·s^{-1} to 5.2×10^{14} cm^{-3}·s^{-1}, 18.2×10^{14} cm^{-3}·s^{-1}, and even 33.7×10^{14} cm^{-3}·s^{-1}. It can be observed that the magnitude of the generation rate is always greater than that of the loss term, and this may explain the increase in O(^{1}D) flux as the O_2 ratio increases from 1% to 20%. Nevertheless, at the O_2 ratio of 50%, the effective acting time and space of the O(^{1}D) generation rate (Fig. 10(a4)) is significantly reduced compared to the case at a lower O_2 ratio. Therefore, although the peaks of the O(^{1}D) generation rate are large, a larger loss rate and a smaller effective acting time and space of the generation term may contribute to a lower O(^{1}D) flux compared to cases with a high ratio of Ar.

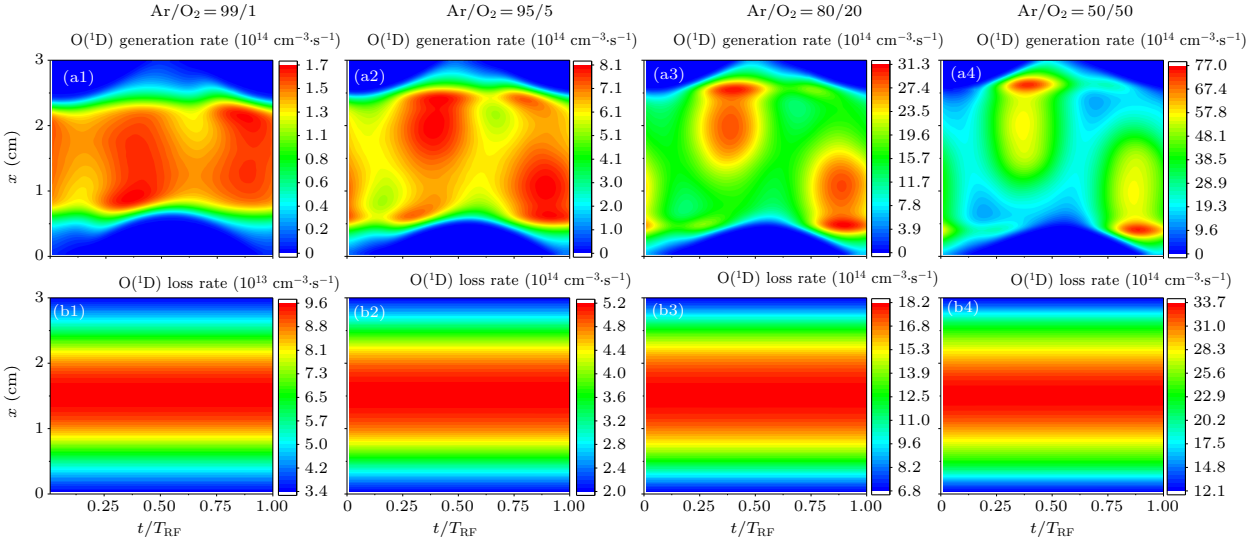


Fig. 10. Spatiotemporal evolutions of (a1)–(a4) O(^{1}D) generation rate (including the reaction rates of R18, R19, R22, R30, R31, R33, R34, and R48), and (b1)–(b4) O(^{1}D) loss rate (incorporating the reaction rates of R24, R25, R49, R51, R52, and R53) as a function of Ar/O_2 gas ratio (99/1, 95/5, 80/20, 50/50). Discharge conditions: Ar/O_2 mixed gases at 200 mTorr with an electrode gap of 3 cm, sustained by 13.56 MHz with 150-V voltage amplitude.

4. Conclusions

The discharges of CCPs operated in Ar/O_2 gas mixtures at 200 mTorr–500 mTorr are investigated using a 1D fluid model coupled with an electron MC model. This investigation focuses on exploring discharge properties, electron dynamics, and the effects of varying physical parameters, including ion densities and neutral fluxes, at different pressures and Ar/O_2 gas ratios.

As the pressure increases, the ion density increases and there is a slight increase in the electron density in the bulk region for a fixed Ar/O_2 gas ratio of 50/50, leading to a slight decrease in the electronegativity, while the discharge mode is always dominated by the DA mode. It is because the discharge exhibits comparatively high electronegativity at an O_2 ratio of 50% under different pressures. Therefore, the drift and ambipolar electric fields are significantly enhanced due to the low electron density and low conductivity in the bulk region, and thus the ionization is dominated by a peak at the sheath collapse edge. Moreover, the O(^{3}P) flux enhances as the pressure increases, which can be easily explained by the increase in density of the background gas. However, the fluxes of O(^{1}D) and Ar* decrease due to the larger loss source terms associated with background gases with the increasing pressure.

With the increase in the proportion of O_2 from 1% to 50%, there is a shift from electropositive to electronegative discharge due to the decrease in electron density and the enhancement of the electronegativity. More specifically, at lower electronegative O_2 ratios, a majority of electrons concentrate in the bulk region, where the electric field is weaker, sheath heating is pronounced, and α mode is dominant. On the contrary, electrons tend to be concentrated at the sheath edge with lower conductivity in the bulk, resulting in a significantly enhanced electric field in the bulk region. Simultaneously, electron heating in the bulk region is enhanced and even comparable to sheath heating. Further, the dominant discharge mode would change from α mode to DA mode. Moreover, O_2-related charged particle densities and O(^{3}P) flux all increase with the increasing O_2 ratio. During the decrease in Ar ratio from 99% to 95%, there is an increase in Ar^+ density due to the enhancement in high-energy electrons involved in ionization. As the Ar ratio continues to decrease, the Ar^+ density will gradually decrease. Ar* flux declines with an increasing proportion of O_2 gas. However, the trends in O(^{1}D) flux show

a slight difference. Taking the result at 200 mTorr as an example, at O_2 ratio below 20%, the rate of $O(^1D)$ production increases due to the addition of O_2 ratio, which further leads to an increase in $O(^1D)$ flux. When the ratio of O_2 exceeds 20%, there is a significant decrease in the effective acting time and space of the $O(^1D)$ production rate, accompanied by a notable increase in the $O(^1D)$ loss rate, both contributing to the reduction in the $O(^1D)$ flux.

In this study, we explored capacitively coupled Ar/O_2 mixed gas discharges powered by a single frequency source. The ion densities and neutral fluxes observed in these discharges can be correlated, to some extent, with electron dynamics and discharge characteristics. In our future work, we plan to investigate a wider range of discharge conditions to establish a comprehensive relationship between discharge parameters, electron dynamics, and transport of the charged as well as neutral particles. Additionally, we aim to combine the etching or deposition profile evolution models to predict the results of the etching or deposition, with the objective of offering valuable guidance to the industry.

Acknowledgements

Project supported by the National Natural Science Foundation of China (Grant Nos. 12020101005, 11975067, and 12347131) and the Fundamental Research Funds for the Central Universities (Grant No. DUT24BS069).

References

[1] Makabe T and Petrović Z 2006 *Plasma Electronics: Applications in Microelectronic Device Fabrication* (London: Taylor and Francis) pp. 3–9
[2] Chabert P and Braithwaite N 2011 *Physics of Radio-Frequency Plasmas* (Cambridge: Cambridge University Press)
[3] Lieberman M A and Lichtenberg A J 2005 *Principles of Plasma Discharges and Materials Processing*, 2nd edn. (New York: Wiley-Interscience) pp. 1–750
[4] Kushner M J 1993 *J. Appl. Phys.* **74** 6538
[5] Dong W, Xu H W, Dai Z L, Song Y H and Wang Y N 2021 *Acta Phys. Sin.* **70** 095213 (in Chinese)
[6] Shinoda K, Miyoshi N, Kobayashi H, Izawa M, Ishikawa K and Hori M 2019 *J. Phys. D: Appl. Phys.* **52** 475106
[7] Jung H, Oh I, Yoon C M, Park B E, Lee S, Kwon O, Lee W, Kwon S, Kim W H and Kim H 2018 *ACS Appl. Mater. Interfaces* **46** 40286
[8] Huang S, Huard C, Shim S, Nam S K, Song I C, Lu S and Kushner M J 2019 *J. Vac. Sci. Technol. A* **37** 031304
[9] Izawa M, Negishi N, Yokogawa K E and Momonoi Y 2007 *Jpn. J. Appl. Phys.* **46** 7870
[10] Qu C, Sakiyama Y, Agarwal P and Kushner M J 2021 *J. Vac. Sci. Technol. A* **39** 052403
[11] Xu X., Li L, Wang S, Zhao L and Ye T 2007 *Plasma Sources Sci. Technol.* **16** 372
[12] Kitajima T, Minowa H and Nakano T 2020 *J. Phys. Commun.* **4** 095013
[13] Nikolić M, Sepulveda I, Gonzalez C, Khogeer N and Fernandez-Monteith M 2021 *J. Phys. D: Appl. Phys.* **54** 275203
[14] Yang Y, Tang C S, Zhao Y F, Yu Y Q and Xin Y 2017 *Acta Phys. Sin.* **66** 185202 (in Chinese)
[15] Krüger F, Lee H, Nam S K and Kushner M J 2021 *Plasma Sources Sci. Technol.* **30** 085002
[16] Zhao Y, Zhou Y, Ma X, Cao L, Zheng F and Xin Y 2019 *Phys. Plasmas* **26** 033502
[17] Greb A, Niemi K, O'Connell D and Gans T 2013 *Appl. Phys. Lett.* **103** 244101
[18] Gudmundsson J T and Snorrason D I 2017 *J. Appl. Phys.* **122** 193302
[19] Gudmundsson J T and Ventéjou B 2015 *J. Appl. Phys.* **118** 153302
[20] Derzsi A, Bruneau B, Gibson A R, Johnson E, O'Connell D, Gans T, Booth J P and Donkó Z 2017 *Plasma Sources Sci. Technol.* **26** 034002
[21] Wang L, Wen D Q, Hartmann P, Donkó Z, Derzsi A, Wang X F, Song Y H, Wang Y N and Schulze J 2020 *Plasma Sources Sci. Technol.* **29** 105004
[22] Wang L, Wen D Q, Zhang Q Z, Song Y H, Zhang Y R and Wang Y N 2019 *Plasma Sources Sci. Technol.* **28** 055007
[23] Lee B J, Lee B J, Efremov A, Yang J W and Kwon K H 2016 *J. Nanosci. Nanotechnol.* **16** 11201
[24] Lee B J, Efremov A, Nam Y and Kwon K H 2020 *Plasma Chem. Plasma Process.* **40** 1365
[25] Tanimura T, Watanabe Y, Sato Y, Kabe Y and Hirota Y 2013 *J. Appl. Phys.* **113** 064102
[26] Kitajima T, Nakano T and Makabe T 2008 *J. Vac. Sci. Technol. A* **26** 1038
[27] Kitajima T, Nakano T and Makabe T 2006 *Appl. Phys. Lett.* **88** 091501
[28] Gogolides E, Vauvert P, Kokkoris G, Turban G and Boudouvis A G 2000 *J. Appl. Phys.* **88** 5570
[29] Fang G Y, Xu L N, Cao Y Q, Wang L G, Wu D and Li A D 2015 *Chem. Commun.* **51** 1341
[30] Kaspar T, Tuan A, Tonkyn R, Hess W P, Rogers J W and Ono Y 2003 *J. Vac. Sci. Technol. B* **21** 895
[31] Wen Y Y, Zhang Y R, Jiang G, Song Y H and Wang Y N 2019 *AIP Adv.* **9** 055019
[32] Singh H, Coburn J W and Graves D B 2000 *J. Vac. Sci. Technol. A* **18** 2680
[33] Kushner M J 1993 *J. Appl. Phys.* **74** 6538
[34] Bhoj A N and Kushner M J 2007 *J. Phys. D: Appl. Phys.* **40** 6953
[35] Sharpless R L and Slanger T G 1989 *J. Chem. Phys.* **91** 7947
[36] Thorsteinsson E G and Gudmundsson J T 2010 *Plasma Sources Sci. Technol.* **19** 055008
[37] Dong W, Zhang Y F, Schulze J and Song Y H 2024 *Plasma Sources Sci. Technol.* **33** 025020
[38] Wang X F, Jia W Z, Song Y H, Zhang Y Y, Dai Z L and Wang Y N 2017 *Phys. Plasmas* **24** 113503
[39] Dong W, Zhang Y F, Dai Z L, Schulze J, Song Y H and Wang Y N 2022 *Plasma Sources Sci. Technol.* **31** 025006
[40] Zhao S X, Gao F, Wang Y N and Bogaerts A 2012 *Plasma Sources Sci. Technol.* **21** 025008
[41] Tinck S, Boullart W and Bogaerts A 2009 *J. Phys. D: Appl. Phys.* **42** 095204
[42] Derzsi A, Hartmann P, Vass M, Horváth B, Gyulai M, Korolov I, Schulze J and Donkó Z 2022 *Plasma Sources Sci. Technol.* **31** 085009
[43] Krishnakumar E and Srivastava S K 1992 *Int. J. Mass Spectrom. Ion Process.* **113** 1
[44] Gudmundsson J T and Lieberman M A 2015 *Plasma Sources Sci. Technol.* **24** 035016
[45] Vasenkov A V, Li X, Oehrlein G S and Kushner M J 2004 *J. Vac. Sci. Technol. A* **22** 511